

GRB 050713A: High Energy Observations of the GRB Prompt and Afterglow Emission

D.C. Morris¹, J. Reeves², V. Pal'shin³, M. Garczarczyk⁴, A.D. Falcone¹, D.N. Burrows¹,
H. Krimm², N. Galante⁵, M. Gaug⁶, S. Mizobuchi⁴, C. Pagani¹, A. Stamerra⁵,
M. Teshima⁴, A.P. Beardmore⁷, O. Godet⁷, N. Gehrels²

ABSTRACT

Swift discovered GRB 050713A and slewed promptly to begin observing with its narrow field instruments 72.6 seconds after the burst onset, while the prompt gamma-ray emission was still detectable in the BAT. Simultaneous emission from two flares is detected in the BAT and XRT. This burst marks just the second time that the BAT and XRT have simultaneously detected emission from a burst and the first time that both instruments have produced a well sampled, simultaneous dataset covering multiple X-ray flares. The temporal rise and decay parameters of the flares are consistent with the internal shock mechanism. In addition to the *Swift* coverage of GRB 050713A, we report on the Konus-Wind (K-W) detection of the prompt emission in the energy range 18-1150 keV, an upper limiting GeV measurement of the prompt emission made by the MAGIC imaging atmospheric Cherenkov telescope and *XMM-Newton* observations of the afterglow. Simultaneous observation between *Swift* XRT and *XMM-Newton* produce consistent results, showing a break in the lightcurve at $T+ \sim 15$ ks. Together, these four observatories provide unusually broad spectral coverage of the prompt emission and detailed X-ray follow-up of the afterglow for two weeks after the burst trigger. Simultaneous spectral fits of K-W with BAT and BAT with XRT data indicate that an absorbed broken powerlaw is often a better fit to GRB flares than a simple absorbed powerlaw. These spectral results together with the rapid temporal rise and decay of the flares suggest that flares are produced in internal shocks due to late time central engine activity.

Subject headings: gamma rays: bursts

1. Introduction

The *Swift* Gamma-Ray Burst Explorer (Gehrels et al. 2004) has been returning unprecedented data about gamma ray bursts (GRBs) for the past

12 months. Of particular interest in the bursts followed by *Swift* has been the early time lightcurve of the afterglows which have shown much greater structure and different temporal decay properties than were expected, leading to much discussion in the literature regarding the nature of the transition between the prompt emission, thought to be due to synchrotron radiation from internal collisions (Gallant et al. 1999) and the afterglow, also thought to be due to synchrotron radiation, though it remains somewhat unclear whether the emission arises in internal or external shocks. *Swift* observations have shown that GRB lightcurves can be described by a canonical 3-segment shape. This shape consists of 1 - an early steep decay phase ($F_\nu \propto \nu^{-\beta} t^{-\alpha}$ where $3 \leq$

¹Department of Astronomy & Astrophysics, 525 Davey Lab., Pennsylvania State University, University Park, PA 16802, USA; morris@astro.psu.edu

²NASA/Goddard Space Flight Center, Greenbelt, MD 20771, USA

³Ioffe Physico-Technical Institute

⁴Max-Planck-Institut für Physik, München, Germany

⁵Dipartimento di Fisica, Università di Siena, and INFN Pisa, Italy

⁶Institut de Física d'Altes Energies, Barcelona, Spain

⁷Department of Physics and Astronomy, University of Leicester, Leicester, LE1 7RH, UK

$\alpha_1 \leq 5$; $t < 500\text{s}$) 2 - a very shallow decay phase ($0.5 \leq \alpha_2 \leq 1.0$; $500\text{s} < t < 10^4\text{s}$) 3 - a 'normal' decay phase ($1 \leq \alpha_3 \leq 1.5$; $10^4\text{s} < t$). (Nousek et al. 2005) Superimposed on this smooth decay profile, Swift has discovered the existence of bright x-ray flares, 2 to 100 times as bright as the underlying afterglow, during the early ($t \leq 10\text{ks}$) stages of GRBs (Burrows et al. 2005b), (Falcone et al. 2006), (Piro 2005), (Romano et al. 2005).

The observation of GRB050117 (Hill et al. 2005) marked the first time that *Swift* slewed to and settled on a GRB while the prompt gamma ray emission was still in progress, arriving 192 seconds after the Burst Alert Telescope (BAT) triggered on the burst which had a T_{90} of 168 seconds. Due to irregularities in the observing mode of the XRT and the proximity of the South Atlantic Anomaly to *Swift* during the observation of GRB050117, however, only very sparse data was collected by the XRT, totaling 11.4 seconds in the first orbit and 946 seconds overall, leaving large gaps in the lightcurve coverage and severely limiting the quality of the spectral analysis that could be performed.

We report here on the observation of GRB 050713A (Falcone et al. 2005), a burst of $T_{90} = 70$ seconds to which *Swift* slewed and began collecting data with the narrow field instruments (NFIs) in just 72.6 seconds, while the prompt gamma ray emission was still detectable by the BAT. This burst marks just the second time that the BAT and XRT have collected simultaneous data on a burst and it marks the first time that both instruments have produced a well sampled, simultaneous dataset covering multiple flares in the prompt emission.

In addition to the *Swift* coverage of GRB 050713A, we report also on prompt and followup observations carried out by Konus-Wind, MAGIC, *XMM-Newton* and ground based optical observatories. In section 2 we describe the observations and data analysis from all instruments including ground follow-up. In section 3 we discuss the implications of the observations in light of the new theoretical understanding emerging from the previously observed *Swift* GRBs. In section 4 we summarize and present our conclusions. Quoted uncertainties are at the 90% level throughout unless otherwise noted.

2. Observations and Data Analysis

Many different observatories and instruments have observed GRB 050713A. We devote the following section to a description of the observations and analysis carried out by each instrument team.

2.1. *Swift* BAT

The *Swift* BAT (Barthelmy et al. 2005) triggered on GRB 050713A at 04:29:02.39 UT, measuring a peak 1-second flux of 6.0 ± 0.4 cts s^{-1} . T_{90} measured in the 15-350 keV energy range is $70 \pm 10\text{s}$ as measured from the BAT trigger time (Palmer et al. 2005). The onset of the burst as defined by the BAT trigger is preceded by a weak, hard (photon index = 1.26) precursor at $T-60\text{s}$. BAT data are processed using the BAT ground software build 11 and BAT Calibration Database files build 11.

At the time of the BAT trigger, the flux rises rapidly and remains elevated during a 12s long, multi-peaked burst. At $T_0+12\text{s}$, the BAT flux rapidly decays with a powerlaw decay rate of $\alpha \sim 8$ for 5 seconds before breaking to a more shallow decay of $\alpha \sim 2.5$ at $T_0+17\text{s}$ (Fig. 4). This decay continues until $T_0+40\text{s}$ at which point the BAT flux has decayed to near background levels. At $T_0+50\text{s}$, a flare is seen with flux $2 \times 10^{-8}\text{ergs cm}^{-2}\text{s}^{-1}$, extrapolated into the XRT 0.2-10.0 keV bandpass, followed by a flare with flux $3.5 \times 10^{-8}\text{ergs cm}^{-2}\text{s}^{-1}$ at $T_0+65\text{s}$, another at T_0+105 with flux $1 \times 10^{-8}\text{ergs cm}^{-2}\text{s}^{-1}$ and some hint of further emission at the onset of a flare seen in the XRT at $T_0+160\text{s}$. A weak but statistically significant precursor is seen at $T_0-70\text{s}$ to $T_0-50\text{s}$ followed by a period of no significant emission from $T_0-50\text{s}$ to the burst trigger.

The spectrum of the entire BAT dataset is well fit with a power-law spectrum with photon index $\Gamma = 1.58 \pm 0.07$, though there is evidence for a slightly harder index of $\Gamma = 1.45$ during the plateau and a softening to $\Gamma = 1.6$ during the rapid decay, and further softening to $\Gamma = 2.0$ during the weak flares. Using the global fit of $\Gamma = 1.58$, the fluence is $9.1 \pm 0.6 \times 10^{-6}\text{ergs cm}^{-2}$ in the 15-350 keV energy range.

2.2. Konus-Wind

GRB 050713A triggered Konus-Wind (K-W) (Aptekar et al. 1995) at $T_0(\text{K-W}) = 04:29:01.745$ UT. It was detected by the S2 detector which observes the north ecliptic hemisphere with an incident angle of $18.^\circ 1$. The propagation delay from Wind to *Swift* is 1.387 s for this GRB. Correcting for this factor, one sees that the K-W trigger time corresponds to $T_0 + 0.742$ s. Prior to $T_0(\text{K-W}) - 0.512$ s data were collected by K-W in a survey mode with lower time resolution of 2.944 s and only 3 broad spectral channels, 18-70keV, 70-300keV and 300-1160keV. From $T_0(\text{K-W})$ to $T_0(\text{K-W}) + 491.776$ s, 64 spectra in 101 channels were accumulated on time scales varying from 64 ms near the trigger to 8.19 s by the time the signal became undetectable. Data were processed using standard Konus-Wind analysis tools and the spectra were fitted by XSPEC 11.3.

Fitting jointly with the BAT data gives $\alpha = 1.29 \pm 0.07$ and $E_{\text{peak}} = 443_{-88}^{+134}$ keV ($\chi^2 = 153$ for 119 d.o.f.). Figure 3 shows that the BAT and Konus data can be well fit to the same model spectrum. A fit to the Band (GRBM) model was also attempted but no statistically significant high energy power-law tail was established. Joint fits between BAT and Konus were also made for other time intervals and will be addressed in greater detail in section 3.3.

The main pulse fluence in the 20 keV to 2 MeV range is $8.08_{-1.77}^{+0.55} \times 10^{-6}$ erg cm^{-2} . The 256-ms peak flux measured from $T_0 + 1.2$ s in the 20 keV to 2 MeV band is $1.34_{-0.45}^{+0.11} \times 10^{-5}$ erg $\text{cm}^{-2} \text{ s}^{-1}$ and the T_{90} durations of the burst in G1, G2, G3 energy bands are 13.3 s, 9.7 and 0.4 s, respectively.

2.3. *Swift* XRT

The XRT (Burrows et al. 2005a) performs an automated sequence of observations (Hill et al. 2004) after *Swift* slews to a GRB detected by the BAT. When the spacecraft first settles on the target, a short image (0.1 s followed by a longer 2.5 s image if a position is not determined in 0.1 s) is taken to determine an accurate position. Following the image, the XRT switches into either Windowed Timing (WT) mode (a high timing accuracy mode with 1 dimensional position information) if the source count rate is above 2 counts s^{-1} , or Photon Counting mode (the more tradi-

tional operating mode of X-ray CCDS in which full 2 dimensional position information is retained but with only 2.5 s timing resolution) if the count rate is below 2 counts s^{-1} .

XRT collected a 0.1 s Image Mode frame upon settling on GRB 050713A 73.4 seconds after the BAT trigger which yields a count rate of 314 counts s^{-1} . Following the Image Mode frame, XRT cascaded down through its automated mode sequence and collected its first WT frame 4.5 seconds later. At the onset of the WT data, the XRT count rate was about 100 counts s^{-1} and decaying as a steady powerlaw. This initial powerlaw decay in the XRT WT data together with the Image Mode data point measured at a flux level ~ 3 times higher just 4.6 s earlier clearly indicates that the XRT settled and began taking data during the latter portion of the flare detected in the BAT at $T_0 + 65$ seconds (see Figure 4). XRT remained in WT mode throughout the entire first orbit of data collection on GRB 050713A, also observing the flare detected by the BAT at $T_0 + 105$ and a lower level flare not clearly detected by the BAT at $T_0 + 155$ s.

Following a 65 minute period of occultation by the Earth, XRT began observations again at $T_0 + 4300$ s, now observing in photon counting (PC) mode since the countrate of the source had decayed below 1 count s^{-1} . A small flare at $T_0 + 10$ ks and the indication of another flare at $T_0 + 45$ ks are seen in the late time XRT lightcurve data, superimposed on an otherwise steady power-law decay. XRT observations continue to monitor the source until $T + 1.8 \times 10^6$ s, a total exposure time of 178 ks, at which time the source had decayed below the XRT detection threshold.

2.3.1. XRT GRB position Analysis

The X-ray afterglow position determined from ground processing of the data is $\text{RA}(\text{J2000}) = 21^{\text{h}}22^{\text{m}}9^{\text{s}}.8\text{Dec}(\text{J2000}) = +77^\circ 4' 29''.0$ with an uncertainty of 3.2 arcseconds. This is 10.5 arcseconds from the reported BAT position, 0.5 arcseconds from the optical counterpart reported by Malesani et al. (Malesani et al. 2005) and 1.5 arcseconds from the initial XRT position calculated onboard the satellite and automatically distributed via the GCN network (Falcone et al. 2005). An X-ray image compiled from the first segment of XRT PC data is shown as Figure 5

with the BAT, XRT and optical counterpart error circles displayed. A faint background source is detected 30 arcseconds due south of the GRB afterglow at a constant flux level of $(7 \pm 2) \times 10^{-4}$ counts s^{-1} . The contribution of this steady source has been removed from the calculation of the afterglow lightcurve.

2.3.2. XRT Temporal Analysis

A timeline of the XRT (as well as other) observations of GRB 050713A is shown in Table 1. The lightcurve will be broadly treated in two parts. Data are processed using the *xrtpipeline* software version 0.9.9. The first part is the initial orbit of data, during which the lightcurve is characterized by bright flares which are simultaneously observed by the BAT as well as the Konus-Wind instrument at higher energies. Due to the extreme variability in this portion of the lightcurve, a global decay index cannot be determined from the XRT data. The second part is the remainder of the XRT data from the second orbit onward, which is characterized primarily by a broken powerlaw decay, though at least one and possibly two small flares are seen superimposed atop this global decay.

First Orbit

Swift finished slewing to GRB 050713A at T+73 s, during the flare which began at T+65 s. The XRT short image frame is collected just after the peak of this flare, at a flux of 1.2×10^{-8} ergs s^{-1} , and the first 20 frames of WT data record the decay of the flare. Fitting a simple powerlaw to this decay from T+79 to T+100 setting T_0 to be the BAT burst trigger time, we find a powerlaw index of 5.6 ± 1.8 (1σ). At T+105 s a new flare begins, which rises with a powerlaw index of 23.3 ± 4.5 for 5-10 s, flattens at the peak of $\sim 9 \times 10^{-9}$ erg s^{-1} for 5-10 s, then decays with a more shallow powerlaw index of 8.4 ± 1.7 for about 30 s. At T+165 s a third flare is detected, which rises with a powerlaw slope of 8.92 ± 3.1 for 5-10 s, flattens at the peak of $\sim 1.5 \times 10^{-9}$ erg s^{-1} for 5-10 s, then decays with a slope of 6.1 ± 1.1 for at least 70 s before the end of the observing window due to Earth occultation.

Second Orbit and Later

The second orbit of data in the XRT is the only single orbit of data in which the afterglow is characterized by a well sampled (greater than 100 events total) lightcurve devoid of any flaring activity. During the 1600 seconds of data in this orbit, from T+4360 s to T+5952 s, the lightcurve decays steadily as a powerlaw with decay index of about 1.0. The third orbit of data is characterized by another flare, beginning at T+10 ks, lasting throughout the entire orbit (about 2ks) and reaching a peak flux of 1×10^{-11} erg s^{-1} . A powerlaw fit to the rising portion of the flare yields a slope of 5.8 ± 1.8 while the decaying portion yields a slope of 11.0 ± 2.5 . Observations were interrupted after 150 s during the fourth orbit due to the occurrence of GRB 050713B, and observations of GRB 050713A remained suspended until T+40 ks. Some suggestion of another flare is seen in the orbit of data beginning at 45 ks, though the statistics are poor. Though afterglow data from the XRT alone do not clearly require a break in the afterglow powerlaw, *XMM-Newton* data (see Figure 7 and §2.4) from T_0+21 ks to T_0+50 ks provide an accurate measure of the late-time decay slope ($\alpha = 1.45$) which cannot fit the XRT data from orbits 2 and 3 without a break in the powerlaw. The joint XRT-*XMM-Newton* lightcurve will be further discussed in §2.4. Table 2 summarizes the flares and their temporal fits.

2.3.3. XRT Spectral Analysis

The XRT spectral analysis of this burst is somewhat complicated by the high degree of flaring activity seen. Data are fit using ancillary response files generated with the *xrtpipeline* task *xrtmkarf* and redistribution response files from the Swift XRT calibration database version 7. In all cases, spectra are binned to a minimum of 20 counts per bin in order to use χ^2 statistics. Fitting the entire first orbit of data, the spectrum is well fit by a highly absorbed powerlaw with photon index = 2.28 ± 0.04 and N_H significantly above the galactic column (1.1×10^{21}) in the direction of GRB 050713A, $N_H = 4.8 \pm 0.2 \times 10^{21}$. We are also able, due to the large number of counts in each of the early flares in the dataset, to fit a spectrum to both the rising and decaying portions of the flares. In doing so we see the typical hard to soft evolu-

tion of the flares (Zhang and Meszaros, 2004). For purposes of the spectral fitting, we have separated the data at 1000 event intervals and produced simple powerlaw fits to each 1000 event interval.

The second orbit of data shows a significantly different spectrum from the first, with a harder spectrum with photon index = 1.9 ± 0.13 and lower value of $N_H = 3.1 \pm 0.43 \times 10^{21}$. The third orbit is well fit by a softer powerlaw similar to that which fit the first orbit with photon index = 2.25 ± 0.23 and $N_H = 4.1 \pm 0.7 \times 10^{21}$.

During the period of overlapping coverage between *Swift* and *XMM-Newton*, XRT has 3.5 ks of exposure time at a mean count rate of 0.04 counts s^{-1} for a total of about 150 events during the simultaneous observing period. Fitting a spectrum to this overlapping coverage yields a photon index = 1.9 ± 0.3 and $N_H = 4.0 \pm 0.15 \times 10^{21}$. The corresponding mean unabsorbed 0.2 – 10.0 keV flux during the overlap period as measured by XRT is $3.4 \pm 0.34 \times 10^{-12}$ ergs $cm^{-2} s^{-1}$.

The data collected after the third orbit are too sparse to justify fitting with higher order models, but a simple absorbed power fit yields a spectrum of photon index = 2.8 ± 0.6 with $N_H = 5.6 \pm 0.2 \times 10^{21}$.

2.4. *XMM-Newton*

XMM-Newton follow-up observations of GRB 050713A commenced 23.6 ks (for the EPIC-PN) and 20.9 ks (for the two EPIC-MOS cameras) after the initial BAT Trigger. The *XMM-Newton* data were processed with the EPPROC and EMPROC pipeline scripts, using the *XMM-Newton* SAS analysis package, version 6.5. A bright rapidly decaying source is detected near the aimpoint of all three EPIC detectors, localized at RA(J2000) = $21^h 22^m 9^s.4$ Dec(J2000) = $+77^\circ 4' 28''.1$. The net exposures after screening and deadtime correction were 24.1 ks (PN) and 27.0 ks (MOS). All three EPIC cameras (PN and 2 MOS) were used in Full Window Mode with the medium filter in place.

Source spectra and lightcurves for all 3 EPIC cameras were extracted from circular regions of $20''$ radius centered on the afterglow. Background data were taken from a $60''$ circle on the same chip as the afterglow, but free of any X-ray sources. Fitting the afterglow lightcurve with a simple power-law decay results in a decay index of $\alpha =$

1.45 ± 0.05 . Several flares are present in the background lightcurve, so as a conservative check, we also excluded times where the background rate is > 0.1 counts s^{-1} . The afterglow decay rate is then $\alpha = 1.39 \pm 0.09$, consistent with the above value. The decay rate from the MOS lightcurve (for the two detectors combined) is also consistent at $\alpha = 1.35 \pm 0.06$.

2.4.1. *XMM-Newton* spectral analysis

Afterglow and background spectra were extracted using the same regions used for the lightcurves, while ancillary and redistribution response files were generated with the SAS tasks ARFGEN and RMFGEN respectively. As with XRT data, source spectra were binned to a minimum of 20 counts per bin in order to use χ^2 statistics. The PN and MOS spectra were fitted jointly, allowing only the cross normalization to vary between the detectors, which is consistent within $< 5\%$. The two MOS spectra and responses were combined to maximize the signal to noise, after first checking that they are consistent with each other. The average net source count rates obtained over the whole observation are 0.58 ± 0.01 counts s^{-1} for the PN and 0.20 ± 0.01 counts s^{-1} per MOS module.

Allowing the absorption column to vary in the spectral fit results in a formally acceptable fit ($\chi^2/dof = 515/496$). The N_H obtained is $3.1 \pm 0.1 \times 10^{21} cm^{-2}$, while the continuum photon index is $\Gamma = 2.07 \pm 0.04$. The time-averaged, absorbed, 0.2-10.0 keV flux obtained for the afterglow is 2.3×10^{-12} erg $cm^{-2} s^{-1}$. These values are consistent with the *Swift* XRT measurement obtained at the time of the *XMM-Newton* observation.

The *XMM-Newton* afterglow spectra were also sliced into three segments of approximately 8 ks in length, in order to search for any spectral evolution within the *XMM-Newton* observation. No change in the continuum parameters was found, all three spectral segments being consistent with a photon index of $\Gamma = 2.1$ and $N_H = 3 \times 10^{21} cm^{-2}$. The spectrum obtained from the PN detector and residuals to an absorbed power-law model (with $\Gamma = 2.08 \pm 0.02$ and $N_H = 3.2 \times 10^{21} cm^{-2}$) are shown in Figure 6.

2.4.2. Joint XMM-Newton and Swift Modeling of the Late Time Afterglow

The power-law decay index obtained from the *XMM-Newton* observation ($\alpha = 1.4$) appears to be steeper than that obtained from the *Swift* XRT in orbit 2 ($\alpha = 1.0$). In order to compare between the *XMM-Newton* and *Swift* afterglow lightcurves, a combined lightcurve from the *XMM-Newton* and *Swift* observations was produced, scaling to the absorbed continuum fluxes measured in the 0.5-10 keV band. The joint *Swift* and *XMM-Newton* lightcurve is shown in Figure 7, zoomed to better display the region at which the lightcurve break occurs.

A single power-law decay slope of $\alpha = 1.20 \pm 0.02$ is an extremely poor fit to the lightcurve in this region, with a fit statistic of $\chi^2/\text{dof} = 201.2/65$. Indeed the lightcurve from $T_0+4\text{ks}$ until $T_0+1000\text{ks}$ after the BAT trigger can be better fitted with a broken power-law. There is a flat decay index of $\alpha = 1.02 \pm 0.07$ at early times and a steeper decay index of $\alpha = 1.45 \pm 0.06$ at later times, with the break in the decay occurring at $25 \pm 3\text{ks}$ after the BAT trigger. The fit statistic is then $\chi^2/\text{dof} = 90.2/59$. The remaining contribution towards the χ^2 originates from two small flares present near $\sim 10\text{ks}$ and $\sim 45\text{ks}$ in the afterglow lightcurve.

2.5. MAGIC

The MAGIC Telescope (Mirzoyan et al. 2005) was able to observe part of the prompt emission phase of GRB 050713A as a response to the alert provided by *Swift*. The observation, at energies above 175 GeV, started at $T_0 + 40\text{ s}$, 20 s after reception of the alert. It overlapped with the prompt emission phase measured by *Swift* and K-W, and lasted for 37 min, until twilight. The observation window covered by MAGIC did not contain the burst onset peak detected at keV-MeV energies, where the *Swift* and K-W spectra were taken. The same region of the sky was observed 48 hours after the burst onset, collecting an additional 49 minutes of data, which was used to determine the background contamination.

The MAGIC (*Major Atmospheric Gamma Imaging Cherenkov*) Telescope is currently the largest single-dish Imaging Air Cherenkov Telescope (IACT) in operation, with the lowest en-

ergy threshold (60 GeV at zenith, increasing with zenith angle). In its fast slewing mode, the telescope can be repositioned within $\sim 30\text{s}$. In case of an alert by GCN, an automated procedure takes only a few seconds to terminate any pending observation, validate the incoming signal and start slewing toward the GRB position, as was the case for GRB 050713A.

Using the standard analysis, no significant excess of γ -like air showers from the position of GRB 050713A above 175 GeV was detected (Albert et al, 2005). This holds both for the prompt emission and during the subsequent observation periods. Figure 8 shows the number of excess events during the first 37 min after the burst, in intervals of 20 s. For comparison, the number of expected background events in the signal region, stable and compatible with statistical fluctuations, is shown. Upper limits to the γ -ray flux are given in Table 3.

This is the first observation of the GRB prompt emission phase performed by an IACT.

2.6. Optical and Other Follow-up Observations

Optical followup observations of GRB 050713A performed by the UVOT and by ground based observatories are summarized in Table 5.

The earliest optical afterglow measurement comes from the RAPTOR-S robotic telescope at the Los Alamos National Laboratory in Los Alamos, New Mexico at $R=18.4 \pm 0.18$ in a coadded series of 8×10 second images with a midpoint observation time of $T_0+99.3\text{s}$ (Wren et al. 2005). A nearly simultaneous measurement was made by the robotic Liverpool Telescope in a coadded series of $3 \sim 2$ minute exposures in the r' band with a midpoint of observation of T_0+3 minutes (Malesani et al. 2005). Later detections below the Digitized Sky Survey limits were reported within the first 60 minutes after the burst trigger in the R band by the Nordic Optical Telescope ($T_0+47\text{m}$), in the I band by the Galileo Italian National Telescope in the Canary Islands and in the infrared J,H, and K bands by the Astronomical Research Consortium Telescope at Apache Point Observatory ($T_0+53\text{m}$).

Due to the bright ($V=6.56$) star HD204408 which is located just 68 arcseconds from the posi-

tion of the burst, the UVOT background level at the position of the afterglow is significantly higher than usual, resulting in abnormally poor sensitivity of the instrument in detecting the afterglow of GRB 050713A. Considering this high background, the non-detection of the afterglow by the UVOT is not surprising.

All other reported optical observations of the afterglow position have yielded only upper limits. Most of the upper limits are near in time to the actual detections but at brighter magnitudes and thus do not produce strong constraints on the decay rate of the optical afterglow. The R-band measurement made at $T_0+10.3$ hours by the Lulin Telescope in Taiwan, however, is at a sufficiently late epoch to place a useful constraint on the optical decay rate. Fitting a simple powerlaw to the two well defined measurements at $T_0+99.3$ s and T_0+180 s and the upper limit at $T_0+10.3$ hours yields an upper limit on the power law decay slope of $\alpha \geq 0.5$, as is shown in Figure 4.

A radio followup observation made with the VLA reports no detection at $T_0+4.3$ days.

3. Discussion

3.1. Multispectral Lightcurve Overview

The Konus-Wind light curve in the 18-1160 keV energy range is similar to the Swift-BAT light curve (see Fig.1). The Konus-Wind three-band light curve is shown in three energy bands in Fig.2. The small precursor peak detected by BAT at $\sim T_0-70$ to T_0-50 s is seen by K-W at statistically significant levels in all three broad, pre-trigger bands: G1 (18-70 keV), G2 (70-300), and G3 (300-1160 keV). The other smaller peaks detected by the BAT after the burst trigger are not seen at statistically significant levels in the K-W data, despite the fact that the peaks at T_0+50 s and at T_0+65 s are more intense in the BAT energy range than the precursor is. The detection by K-W of the precursor but not the later flares is indicative of the harder spectral index seen in the precursor as compared to the later flares (see section 3.3 for discussion of separate spectral fits to individual flares).

The XRT lightcurve with BAT data overplotted is shown in Figure 4. Both the X-ray and gamma-ray data in the first orbit are dominated by flaring activity, making it difficult to draw a

conclusion regarding the underlying powerlaw decay index from this orbit alone. The XRT data beginning at T_0+4 ks (orbit 2) and extending until T_0+40 ks show a significantly flatter powerlaw decay slope of -0.8, implying that a break in the powerlaw decay has occurred near the end of the first orbit of XRT coverage at $\sim T_0+300$ s and that a period of energy injection occurs from $\sim T_0+300$ s to $\sim T_0+15$ ks. Another break in the lightcurve then occurs between T_0+15 ks and T_0+40 ks to a steeper, "normal", pre-jetbreak decay slope, as shown by the *XMM-Newton* data ($\alpha \sim 1.4$). Support for this notion of the presence of an energy injection phase may be drawn from the differing X-ray spectral parameters derived for the second orbit of XRT data as compared to the prompt flaring emission and the later time emission from orbit 3 onward (see Table 5). *XMM-Newton* data coverage nicely fills much of the data gap in the XRT coverage between T_0+15 ks and T_0+40 ks and provides high signal to noise data in this regime, producing a confident determination of the lightcurve break.

The global picture of the lightcurve of this burst is one in which the early data (prior to T_0+12 s) shows a bright plateau in the 15 keV to 1 MeV energy range, consisting of multiple overlapping peaks. At T_0+12 s the emission drops rapidly, consistent with a curvature radiation falloff (Zhang and Meszaros, 2004) until subsequent flaring activity begins to be seen in the 0.2-150 keV region with some indication of flux at higher energies from Konus-Wind. The earliest ground based optical detections are reported at this time also, suggesting that the flares may also be optically bright, though we do not have sufficient timing resolution in the optical data to confirm this speculation. Due to the rapid rise and decay of the flares, internal shocks from continued central engine activity appears to be the most likely explanation for these flares (Ioka et al. 2005). Following this prompt emission phase, an energy injection phase begins which dominates the lightcurve until at least T_0+16 ks. During the energy injection phase, continued activity of the central engine adds energy to the afterglow of the burst, either through additional ejection events or through the realization of energy contained in previously ejected outward moving relativistic shells which only collide at later times, producing late

time internal shock emission which is then added to the overall decay (Zhang et al., 2005). It may be expected, if the energy injection phase is due to continued central engine activity, that flaring behavior would continue to be observed during this period and, indeed, some evidence for small scale flaring activity during both the second and third orbit of XRT data can be seen, though at a much reduced significance in comparison to the flaring activity of the first orbit. Near T_0+25 ks, the energy injection phase ends, giving way to a steeper decay slope similar to what is often seen in GRBs prior to the presence of a traditional jet-break (Nousek et al. 2005).

3.2. Flares

Many flares superimposed on top of the overall decay of GRB 050713A show the typical properties seen in other bursts that $\delta t/t \sim 1$ and the peak flux level is negatively correlated with the time of the flare (Falcone et al, 2005, Berger et al, 2005). These two properties of flares seen in *Swift* GRB afterglows have been cited as evidence for flares being produced through accretion processes onto the central compact object (Perna, Armitage and Zhang, 2006), but we offer here that the constancy of the $\delta t/t$ value of flares may only be a by-product of the overall decay of the afterglow in so much as the sensitivity of the XRT to flares is naturally degraded as the overall flux level of the afterglow decays, thus *requiring* flares at later times (and hence, lower flux levels) to be longer in duration for enough counts to be collected to produce a significant flare seen above the background. Such a case can be seen in comparing the early time flares in the first orbit of GRB 050713A to the flare seen in the the third orbit. During the first orbit, the underlying flux level beneath the flares is poorly determined, but can be assumed to be 10-100 cts/s. We are dominated in this portion of the lightcurve by the Poissonian error in the flux, which, in a 1 second integration will be 3.33-10 cts/s, or 10-33% . Thus, for a flare to appear at the 6 sigma level above the background during this portion of the lightcurve, at most 60 counts above the normal powerlaw decay are needed, which can be easily acquired in 1s by a simple doubling of the count rate. During the third orbit, however, the underlying afterglow flux level has dropped to ~ 0.1 cts/s. During a 1

second integration at 0.1 cts/s the Poisson error alone is 0.3 cts/s, so for a flare to be detectable at 6 sigma above background at these count levels, the rate would need to increase from 0.1cts/s to 1.9cts/s, a 19 fold increase, which has been seen only in the very brightest flares. In order to be sensitive to the same 2 fold increase in flux level as during the first orbit, the flare which occurs at a flux level of 0.1 cts/s needs to have a Poission error which is 1/6 of the total counts in the observation, ie, 36 counts must be collected, which implies an exposure time of 360s at this countrate. Thus, we see that in moving from the first orbit at 100s to the third orbit at 10000s assuming a typical underlying powerlaw decay of the afterglow of $\alpha \sim 1$, we have decreased the temporal resolution of XRT to detect flares by a factor of 360. This is not to imply that there is not another more physical cause for the constancy of the $\delta t/t$ ratio seen in flares, but rather to note that the typical GRB seen by the *Swift* XRT does not provide sufficient flux at times typically greater than a few ks to detect the shorter timescale flares that are so often seen during the first orbit.

In GRB 050713A, a faint, short flare seems to appear in the XRT data at T_0+45 ks, though the statistics are, predictably, poor. This time is overlapped by *XMM-Newton* data, though, so we can look for evidence of the short flare in the *XMM-Newton* data. In Figure 9 we show the *XMM-Newton* lightcurve, plotted linearly and zoomed near T_0+45 ks. Indeed, a 1-2 sigma deviation above the background decay is seen at T_0+45 ks, though evidence of this deviation being a flare similar to those seen at earlier times remains uncertain.

3.3. Joint Spectral Fitting

Due to the relatively narrow spectral response function of the BAT (15-150 keV for mask-tagged events) and the XRT (0.2-10keV), a spectral fit to data from only one of the two high energy instruments on *Swift* is usually not able to discriminate between various higher order spectral models. Analysts and authors are usually limited to choosing between a power-law or Band function. In GRB 050713A we have a rare case of data coverage overlap between BAT and XRT (0.3-150 keV) and also between BAT and Konus-Wind (15keV-4MeV). Taking advantage of this where appro-

appropriate, considering the relative flux levels in the three instruments, we have jointly fitted spectral datasets between the two pairs of instruments. During the precursor and from T_0+0 to $T_0+16.5$ s, we perform joint fitting between BAT and Konus-Wind data. From $T_0+16.5$ to T_0+78 s we have only BAT data. From T_0+78 to T_0+116 s and during the onset of the flare at T_0+160 we perform joint fitting between XRT and BAT. We have grouped the data into segments (as shown in Table 4) in order to separate temporal regions of data which we expect may show significantly different spectral parameters. Segments 1-4 contain BAT and Konus-Wind data and are segmented to separate prompt emission from the rapid decay phase. Segments 5-10 contain XRT and BAT data and are segmented to distinguish the 3 flares which have overlapping data and also to separate the rise of each flare from the decay of each flare.

3.3.1. Segment 1: precursor ($T-65$ to $T-55$ s)

The precursor is the most poorly sampled of all the regions. Despite the low number of counts in the region, a cutoff powerlaw is favored over a single powerlaw at 90% confidence according to the F-test. Of all the segments fit, the precursor has the hardest photon index, regardless of the model which is used to perform the fits.

3.3.2. Segment 2: prompt emission plateau (T_0+0 to $T_0+8.5$ s)

The plateau of the prompt emission is strangely not well fit by any of the models used. The cutoff powerlaw is the best fit model, though with a poor χ^2 value of 1.60. Next to the precursor, the prompt plateau has the second hardest photon index of all segments fit, regardless of the model used.

3.3.3. Segment 3: rapid decay ($T_0+8.5$ to T_0+25 s)

As with the other data segments which contain K-W data, the rapid decay segment is poorly fit by a simple powerlaw and is best fit by a cutoff powerlaw. The photon index of the cutoff powerlaw in segment 3 is quite similar to that in the prompt plateau, but the cutoff energy is significantly lower (312 keV compared to 760keV in the

plateau), suggesting that the highest energy flux is "shutting off" during the rapid decay phase.

3.3.4. Segment 4: plateau + early rapid decay (T_0+0 to $T_0+16.5$ s)

This segment is an extension of the prompt segment to slightly later times, encompassing slightly more data. The cutoff powerlaw is the best fit with a photon index similar to segments 2 and 3 and a cutoff energy between those in segments 2 and 3.

3.3.5. Segment 5: rise of T_0+60 flare (T_0+59 to T_0+68 s)

This segment contains only BAT data and is included for completeness, though the narrowness of the BAT spectral response limits the ability to discern between models. A simple powerlaw fit is a good fit with photon index of 1.83. NH is unconstrained. We note, however, that a powerlaw plus blackbody model is also a good fit to this segment.

3.3.6. Segment 6: decay of T_0+60 flare (T_0+68 to T_0+95 s)

Only in this segment, the data time ranges are mismatched between XRT and BAT (due to XRT observations beginning towards the end of the flare decay). Rather than ignore this flare or consider only the later part of the flare decay where XRT and BAT data coverage overlap, we have chosen to fit the entire BAT time range from T_0+68 to T_0+95 s together with the T_0+79 to T_0+95 s XRT data (note that the Image mode data taken at T_0+73 s is highly piled up and cannot be used spectrally) for consistency with our treatment of the other flares. A simple powerlaw is a good fit to this segment, yielding an NH of $5.2 \times 10^{21} \text{cm}^{-2}$ and a photon index of 2.47, significantly softer than the rise of the flare, as expected.

3.3.7. Segment 7: rise of T_0+100 flare (T_0+100 to T_0+113 s)

In the rise of the brightest flare seen in XRT, both a absorbed powerlaw plus blackbody model and a absorbed broken powerlaw model are significantly better fits (F-test probability $3e-4$) than a simple absorbed powerlaw. The powerlaw plus blackbody indicates a very large NH of $1.2 \times 10^{22} \text{cm}^{-2}$ and a relatively soft photon index of 2.0

with a blackbody temperature of $kT=0.01$ keV. The absorbed broken powerlaw indicates N_H of $4.3 \times 10^{21} \text{cm}^{-2}$ and photon indices of 1.26 and 2.01, broken at 3.4 keV. These two models are somewhat degenerate in this dataset, with both models producing a roll over in flux at low (below 0.5 keV) and high (above 50 keV) energies.

3.3.8. Segment 8: decay of T_0+100 flare (T_0+113 to T_0+150 s)

The decay portion of this flare is well fit by a simple absorbed powerlaw with N_H of $6.0 \times 10^{21} \text{cm}^{-2}$ and photon index of 2.68. We note, however, that both a absorbed broken powerlaw and absorbed powerlaw plus blackbody are equally good fits to the data.

3.3.9. Segment 9: rise of T_0+160 flare (T_0+159 to T_0+171 s)

The rise of the last flare with overlapping data is well fit by a simple absorbed powerlaw with N_H $5.4 \times 10^{21} \text{cm}^{-2}$ and photon index of 2.52, however the absorbed powerlaw plus blackbody is, strictly, a better fit according to the ftest, though only at about the 80% confidence level (ftest probability = 0.219), with N_H of $5.0 \times 10^{21} \text{cm}^{-2}$, $kT=200$ keV and photon index of 2.43.

3.3.10. Segment 10: decay of T_0+160 flare (T_0+171 to T_0+200 s)

The decay of this flare is well fit by a absorbed powerlaw with N_H of $3.8 \times 10^{21} \text{cm}^{-2}$ and photon index of 2.55, though as with segment 9, the absorbed powerlaw plus blackbody is also an acceptable fit with N_H of $4.4 \times 10^{21} \text{cm}^{-2}$, $kT=5.2$ keV and photon index of 2.83. It should be noted that the BAT flux is very near the noise level in this segment and really provides only an upper limit on the spectral fitting process in the higher energy region.

3.4. Broadband SED

We have produced the broadband SED of the afterglow of GRB 050713A over the time range from T_0+20 s to T_0+1000 s (Figure 10). This timerange includes detections of the burst afterglow in the optical from the RAPTOR-S and Liverpool telescopes and in the X-ray from *Swift* BAT and XRT. It also includes upper limits in the γ -ray

energy range from K-W (whose detectable emission ends at $T_0+\sim 10$ s) and in the GeV energy range from MAGIC. A similar SED has been addressed by the MAGIC collaboration in their paper regarding the MAGIC flux upper limit (Albert et al. 2006) in which they note that the SED composed of data from *Swift* and MAGIC (0.2keV to 400GeV) is consistent with a single, absorbed, unbroken powerlaw. We confirm this result, citing best fit parameters for such a single powerlaw fit of $N_H = 4.6 \times 10^{21} \pm 6 \times 10^{20} \text{cm}^{-2}$ and photon index = 1.82 ± 0.07 and a reduced $\chi^2 = 1.29$.

We add that a single absorbed powerlaw fit is not, however, consistent with the data when we also consider the contemporaneous optical detections. The relative faintness of the optical detections compared to the X-ray detections combined with the upper limits from K-W and MAGIC requires at least one break in the spectral slope. Figure 10 shows the best fit to the entire SED using an absorbed powerlaw (dotted), absorbed broken powerlaw (solid) and absorbed Band function (dashed). The spectral parameters and fit characteristics for each of these fits are shown in Table 6. We have not corrected for the attenuation of flux above 10GeV due to photonphoton interactions with the infrared background (de Jager and Stecker 2002), (Kneiske et al. 2004), (Primack, Bullock and Somerville 2005), however, our spectral fit results will remain valid independent of this effect due to the constraints placed by the K-W limiting flux measurement from 20keV to 4MeV.

4. Summary

GRB 050713A is one of the rare bursts observed simultaneously in soft X-rays (XRT), hard X-rays (BAT) and gamma-rays (Konus-Wind). The broad spectral coverage of these simultaneous measurements has allowed us to test the early prompt emission, rapid decay, and several flares in the early emission with several different spectral models. In general we find a cutoff powerlaw model to be a good fit to segments with data extending into the MeV range, thus able to constrain the high energy component of the model. For data segments with 0.3-150 keV coverage (BAT and XRT data) we find that a simple absorbed powerlaw is often an adequate fit to the data, though an absorbed powerlaw plus blackbody or absorbed

broken powerlaw model seems to sometimes be a marginally better fit during periods of flaring activity.

The lightcurve structure of GRB 050713A is quite typical of many GRBs that have been observed by *Swift*. It has an early section showing steep decay slopes of $\alpha > 5$ and bright flares extending until ~ 1 ks, followed by a break to a flatter section with decay slope $\alpha \sim 1.0$ lasting until ~ 40 ks, followed by a break to a steeper slope of $\alpha = 1.45$.

We have temporally separated the early, flaring portion of the burst into 10 segments and attempted to fit each segment using 4 different spectral models, 1) an absorbed powerlaw 2) an absorbed cutoff or broken powerlaw (cutoff for data extending beyond 150keV, broken otherwise) 3) an absorbed Band function and 4) an absorbed blackbody plus powerlaw. In all segments where at least two instruments provide significant, simultaneous levels of emission, and hence the spectral data span more than 2 decades in energy, we find that at least one of the higher order spectral models is acceptable and, in several cases, is a better fit to the data than a simple absorbed powerlaw. This suggests that the spectral shape of GRB flares, while consistent with a simple absorbed powerlaw when viewed through any particular narrow spectral window, is intrinsically fit in the broadband by a model with attenuated flux above (and possibly below) some threshold energy.

It has long been known that GRB prompt emission is better fit by spectral models with a high (and sometimes low) energy cutoff than by a simple absorbed powerlaw (Ryde 2005) (Band et al. 1993), and thus the indication that GRB flares are fit by a similar spectral model is suggestive of similar emission mechanisms responsible for the production of flares and for the prompt emission itself, namely internal shocks produced as a result of central engine activity. Since the discovery of X-ray flares in GRBs by *Swift*, relatively few of the flares have been observed simultaneously across a broad enough energy range to determine whether such higher order models are necessary to fit their spectra, making the multi-instrument observations of GRB 050713A unique and valuable.

We have also examined the temporal properties of the flares seen in GRB 050713A as early as T_0+80 s and as late as T_0+10 ks. In all cases

we find the flares to have steep powerlaw rise and decay slopes and $0.1 < \delta t/t < 1$, which also suggests internal rather than external shocks as the production mechanism for the flares (Burrows et al. 2005b) (Ioka et al. 2005).

We have furthermore discussed the difficulty that *Swift* XRT will face in detecting late time flaring activity, and in particular late, short timescale flaring activity due to the low relative XRT count rates typically involved. GRB 050713A has simultaneous coverage at moderately late times with *XMM-Newton* which has allowed us to search for short, faint flares in the *XMM-Newton* data where there is the hint of such activity in the XRT lightcurve. No conclusive evidence of flaring in the *XMM-Newton* data has been found.

Finally, we have created a broadband SED of the flaring region of GRB 050713A from 0.002keV to 500GeV from T_0+20 s to T_0+1000 s. We find that the SED is inconsistent with a single absorbed powerlaw and is best fit by an absorbed broken powerlaw. This overall SED again implies that GRB flares are best fit by a spectral model similar to that of the prompt emission itself and thus suggests a common mechanism for the emission from the prompt phase and from flares.

This work is supported at Penn State by NASA contract NAS5-00136. We gratefully acknowledge the contributions of dozens of members of the *Swift* team at PSU, University of Leicester, OAB, GSFC, ASDC, MPE and our subcontractors, who helped make this Observatory possible and to the Flight Operations Team for their support above and beyond the call of duty. This work contains observations obtained with *XMM-Newton*, an ESA science mission with instruments and contributions directly funded by ESA member states and the USA (NASA).

REFERENCES

- Albert, J., et al., 2006, astro-ph0602231
- Aptekar, R.L., et al., 1995, Space Sci. Rev., 71, 265
- Band, D., et al., 1993, ApJ, 413, 231
- Barthelmy, S., et al., 2005, Space Sci. Rev., 120, 143

- Berger et al., 2005, ApJ, submitted
- Burrows, D.N., et al., 2005a, Space Sci. Rev., 120, 165
- Burrows, D.N., et al., 2005b, Science, 309, 1833
- Dickey, J.M. and Lockman, F.J., 1990, ARA&A, 28, p215
- Falcone, A.D., et al., 2005, GCN 3581
- Falcone, A.D., 2006, ApJ, accepted, astro-ph0512615
- Gallant, Y.A., et al, 1999, A&AS, 138, 549G
- Gehrels, N., et al., 2004, ApJ, 611, 1005
- Hill, J.E., et al., 2004, Proc. SPIE, Vol. 5165, 217
- Hill, J.E., et al., 2005, astro-ph0510008
- Ioka, K., et al., 2005, ApJ, 631, 429
- de Jager, O.C. and Stecker, F.W. 2002, ApJ, 566, 738
- Kneiske, T. M., et al., 2004, A&AS, 413, 807
- Kraft, R.P., Burrows, D.N., Nousek, J.A., 1991, ApJ, 344, 355
- Kouveliotou, C., Meegan, C.A., Fishman, G.J., Bhat, N.P., Briggs, M.S., Koshut, T.M., Paciesas, W.S., Pendleton, G.N., 1993, ApJ, 413:L101, L104
- Malesani, D., et al., 2005, GCN 3582
- Mirzoyan, R. et al., 2005, IP Procs 29th ICRC
- Nousek, J.A., et al, 2005, astro-ph0508332
- Palmer, D.M., et al., 2005, GCN 3597
- Perna, R., Armitage, P.J., Zhang, B., 2006, ApJ, 636, 29
- Piro, L., 2005, astro-ph0506020
- Primack, J.R., Bullock, J.S., Somerville, R.S. 2005, AIP Conf. Proceedings # 745, p23
- Romano, P., et al., 2006, ApJ, accepted, astro-ph0601173
- Roming, P., et al., 2005, Space Sci. Rev., 120, 95
- Ryde, F., 2005, ApJ, 625, 95
- Schlegel, D.J., Finkbeiner, D.P., and Davies, M., 1998, ApJ, 500, 525
- Wren, J., et al., 2005, GCN 3604
- Zhang, B. and Meszaros, P., 2004, IJoMP A, v19, 15, 2385
- Zhang, B., et al., 2005, astro-ph0508321

This 2-column preprint was prepared with the AAS L^AT_EX macros v5.2.

TABLE 1
A SUMMARY OF HIGH ENERGY OBSERVATIONS OF GRB 0500713A

Observatory /Instr	Start Time (UT)	Stop Time (UT)	Live-time (Seconds)	Time Since BAT Trigger (Seconds)
Swift-BAT	04:29:02.4	04:32:00	178	0
Swift-XRT	04:30:14	04:37:02	408	73
MAGIC(limit)	04:29:42	05:06:45	2223	40
Konus-Wind	04:29:01.7	04:37:13.4	491.8	0
XMM-Newton	10:17:00	18:22:00	20900	27000

TABLE 2
GRB 050713A: X-RAY FLARES PARAMETERS.

Start Time (s)	Stop Time (s)	Duration (s)	Rise (unitless)	Decay (unitless)	Peak Flux (ergs/cm ² /s)
79s	101s	22s	NA	5.6 +/- 1.8	3x10 ⁻⁸ (from BAT)
101s	161s	60s	23.3 +/- 5	8.4 +/- 1.8	9x10 ⁻⁹
161s	304s	143s	8.9 +/- 3	6.1 +/- 1.2	1.5x10 ⁻⁹
9751s	11840s	2089s	5.76 +/- 1.8	11.0 +/- 2.4	1x10 ⁻¹¹

TABLE 3
MAGIC UPPER LIMIT (95% CL) ON GRB 050713A BETWEEN $T_0 + 40$ s AND $T_0 + 130$ s. LIMITS
INCLUDE A SYSTEMATIC UNCERTAINTY OF 30%. 1 C.U. (*Crab Unit*) =
 $1.5 \times 10^{-6} \times (E/\text{GeV})^{-2.58} \text{ ph/cm}^2/\text{s}/\text{GeV}$.

Energy (GeV)	Excess evts. (uplim)	Eff. Area (x10 ⁸ cm ²)	Flux lim (cm-2keV-1s-1)	Flux lim (C.U.)
175 – 225	8.5	1.7	1.3×10^{-17}	7.6
225 – 300	10.4	3.4	3.9×10^{-18}	4.8
300 – 400	6.0	5.3	1.6×10^{-18}	3.8
400 – 1000	4.3	6.5	2.3×10^{-19}	3.3

TABLE 4

GRB 050713A: JOINT SPECTRAL FITS. REGIONS 1-10 COVER TIMERANGES $T_0 + \delta T$ WHERE δT IS : 1: -70s - -49.5s 2: 0s - 8.5s 3: 8.5s - 25s 4: 0s - 16.5s 5: 59s - 68s 6: 68s - 95s 7: 100s - 113s 8: 113s - 150s 9: 159s - 171s 10: 171s - 200s. IN SEGMENTS WHERE A PARTICULAR MODEL WAS UNAPPLICABLE OR THE FIT DID NOT CONVERGE, NA IS ENTERED IN THE TABLE.

Param	1	2	3	4	5	6	7	8	9	10
pl:NH	NA	NA	NA	NA	NA	0.52	0.59	0.60	0.54	0.38
pl:PhInd	1.26	1.44	1.61	1.47	1.83	2.47	1.72	2.68	2.52	2.55
pl: χ^2	1.54	1.96	1.39	1.95	0.98	1.20	1.21	1.07	1.04	1.00
pl:dof	12	101	91	98	26	74	98	125	22	37
Cutoff:PhInd	0.913	1.27	1.31	1.29	NA	NA	NA	NA	NA	NA
Cutoff:HighE	4e5	760	312	622	NA	NA	NA	NA	NA	NA
Cutoff: χ^2	1.20	1.60	1.02	1.29	NA	NA	NA	NA	NA	NA
Cutoff:dof	11	110	90	100	NA	NA	NA	NA	NA	NA
bknpl:NH	NA	NA	NA	NA	NA	0.58	0.43	0.45	NA	NA
bknpl:ph1	NA	NA	NA	NA	0.95	2.69	1.26	1.93	NA	NA
bknpl:break	NA	NA	NA	NA	5.8	4.1	3.4	1.8	NA	NA
bknpl:ph2	NA	NA	NA	NA	2.1	1.5	2.0	2.8	NA	NA
bknpl: χ^2	NA	NA	NA	NA	1.06	1.31	1.03	1.04	NA	NA
bknpl:dof	NA	NA	NA	NA	23	73	97	124	21	36
Band:NH	NA	NA	NA	NA	NA	0.33	0.49	0.54	0.41	0.33
Band: α	-1.13	-1.27	-1.27	-1.29	-2.01	-1.69	-1.46	-2.32	-1.98	-2.17
Band: β	-1.26	-9.36	-2.39	-9.29	-9.07	-1.88	-9.36	-9.32	-9.04	-8.78
Band:T	101	761	244	636	994	10.6	30.7	10.6	10.6	10.6
Band: χ^2	1.85	1.61	1.03	1.28	1.06	2.11	1.11	1.13	1.26	1.12
Band:dof	10	109	89	101	23	73	97	124	21	36
pl+bb:NH	NA	NA	NA	NA	NA	0.59	1.17	0.63	0.50	0.44
pl+bb:kT	3.59	59.4	26.4	44.97	NA	7.1	0.1	4.4	200	5.2
pl+bb:kT _n	0.068	2.74	0.46	1.47	NA	0.07	2.48	0.01	2.90	0.01
pl+bb:PhInd	1.00	1.64	1.76	1.63	NA	2.75	2.00	2.77	2.43	2.83
pl+bb:PhInd _n	0.053	13.97	7.69	11.65	NA	1.53	2.32	2.03	0.51	0.44
pl+bb: χ^2	1.15	1.79	1.03	1.60	NA	1.33	1.04	1.07	0.90	0.98
pl+bb:dof	10	109	89	101	NA	73	97	124	21	36

TABLE 5
GRB 050713A: GROUND BASED OPTICAL FOLLOWUP.

Observatory	Time	Band	Magnitude/Limit
McDonald Obs, Tex	T ₀ +22.4s	unfilt	17.7 (lim)
RAPTOR_S, LANL	T ₀ +99.3s	R	18.4 +/- 0.18
Liverpool Robotic Telescope, Liverpool	T ₀ +180s	r'	19.2
<i>Swift</i>	T ₀ +252s	V	17.98
<i>Swift</i>	T ₀ +309s	U	17.81
<i>Swift</i>	T ₀ +311s	UVM2	17.13
<i>Swift</i>	T ₀ +325s	UVW1	16.85
<i>Swift</i>	T ₀ +326s	UVW2	17.08
<i>Swift</i>	T ₀ +351s	B	18.08
Red Buttes Obs, Wy	T ₀ +27m	R	19.4 (lim)
Red Buttes Obs, Wy	T ₀ +31m	I	18.2 (lim)
Nordic Optical Tel	T ₀ +47m	R	< DSS limit
Galileo National Telescope, Canary Islands	T ₀ +48m	I	< DSS limit
ARC Telescope, Apache Point Obs	T ₀ +53m	J,H,K	detected
Red Buttes Obs, Wy	T ₀ +93m	R	19.4 (lim)
Red Buttes Obs, Wy	T ₀ +98m	I	18.7 (lim)
Lulin Telescope, Taiwan	T ₀ +10.3h	R	22.4 (lim)
VLA, NRAO	T ₀ +4.3d	8.5 GHz	96 microJan

TABLE 6
GRB 050713A: SED FIT DATA.

Param	Value	Error/dof
PL:NH	2.8×10^{20}	...
PL:PhInd	1.29	...
PL: χ^2	7.2	65
BknPL:NH	3.36×21	6×20
BknPL:PhId1	0.78	0.10
BknPL:BreakE	2.33	1.1
BknPL:PhInd2	2.02	0.22
BknPL: χ^2	1.28	63
Band:NH	2.58×21	3×20
Band: α	-0.91	0.04
Band: β	-2.256	0.25
Band:T	10.0	10.0
Band: χ^2	1.65	63

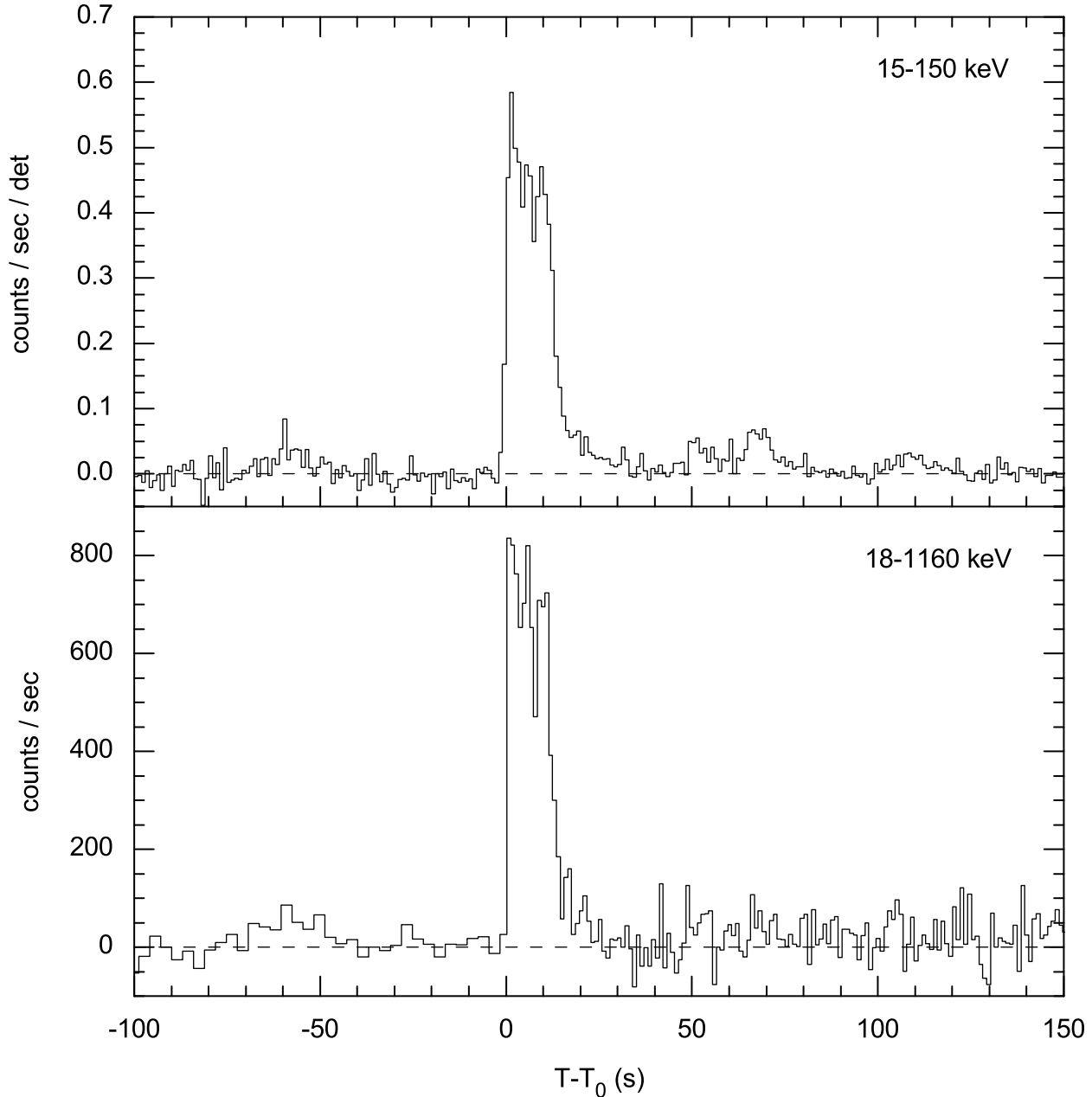


Fig. 1.— Background subtracted BAT (top panel) and Konus-WIND (bottom) light curves on the same time scale. The plots have been adjusted so that the trigger time for both plots is the same relative to the burst. T_0 in the lower plot is $T_0(\text{BAT})$ plus the propagation time between the spacecrafts (0.742 s). BAT data are binned to 1 s resolution throughout. K-W data are binned to 2.94 s resolution in survey mode prior to the burst trigger and are binned to 1 s resolution in GRB follow-up mode after the trigger. Note that the precursor at T_0-65 s is detected in both BAT and K-W while post-trigger flares seen in the BAT at T_0+50 s, T_0+65 s and T_0+105 s are not clearly detected by K-W. This suggests a harder spectrum of the precursor than the post-trigger flares, which is confirmed by joint BAT/K-W spectral fits. The main burst consists of 3 closely spaced, overlapping pulses in both the BAT and K-W energy ranges. The K-W lightcurve decays rapidly to background level by T_0+15 s while the BAT lightcurve continues to show low level emission out to $T_0+\sim 200$ s.

KONUS-WIND GRB 050713a
 $T_0 = 16141.745$ s UT (04:29:01.745)
S2

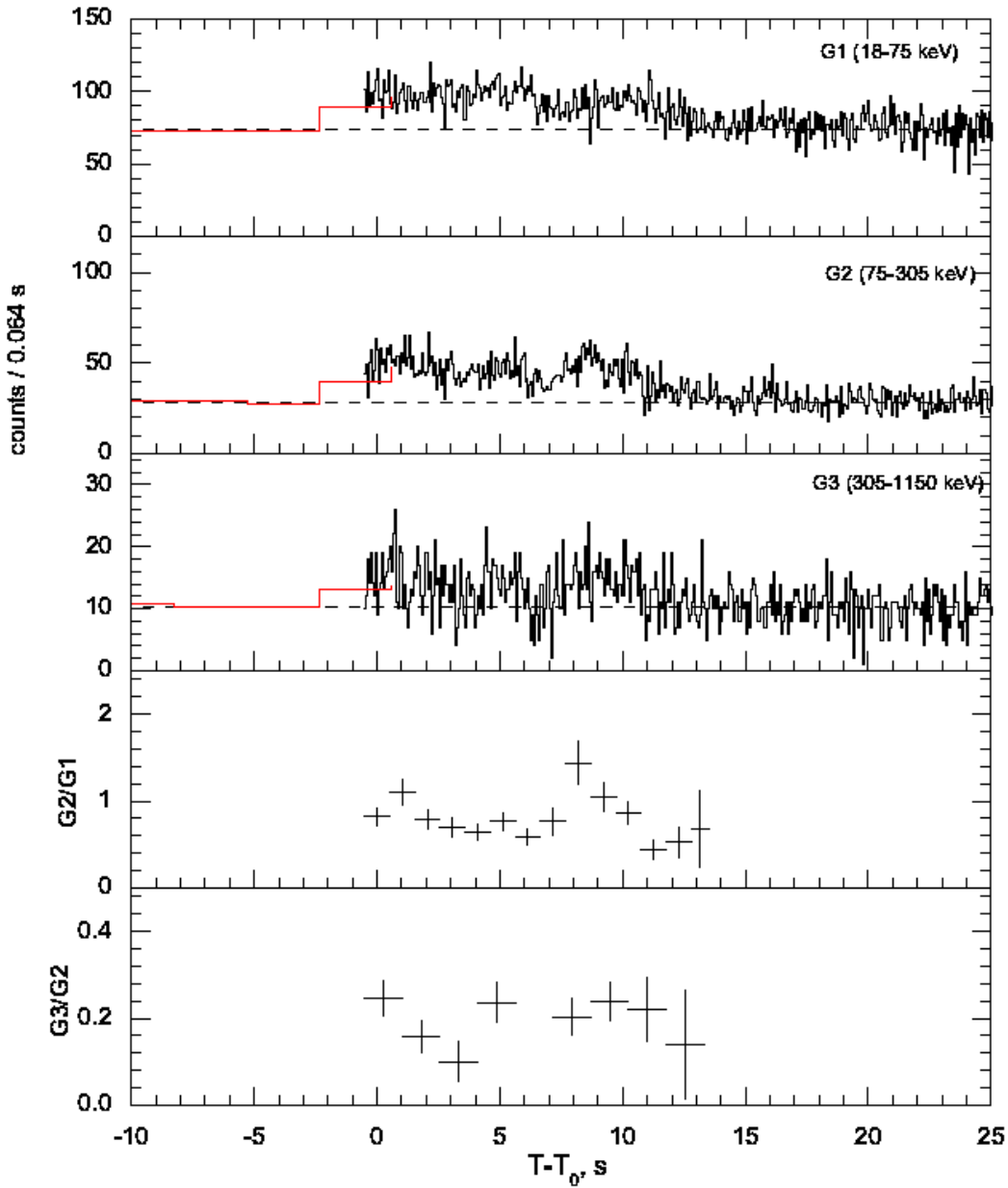
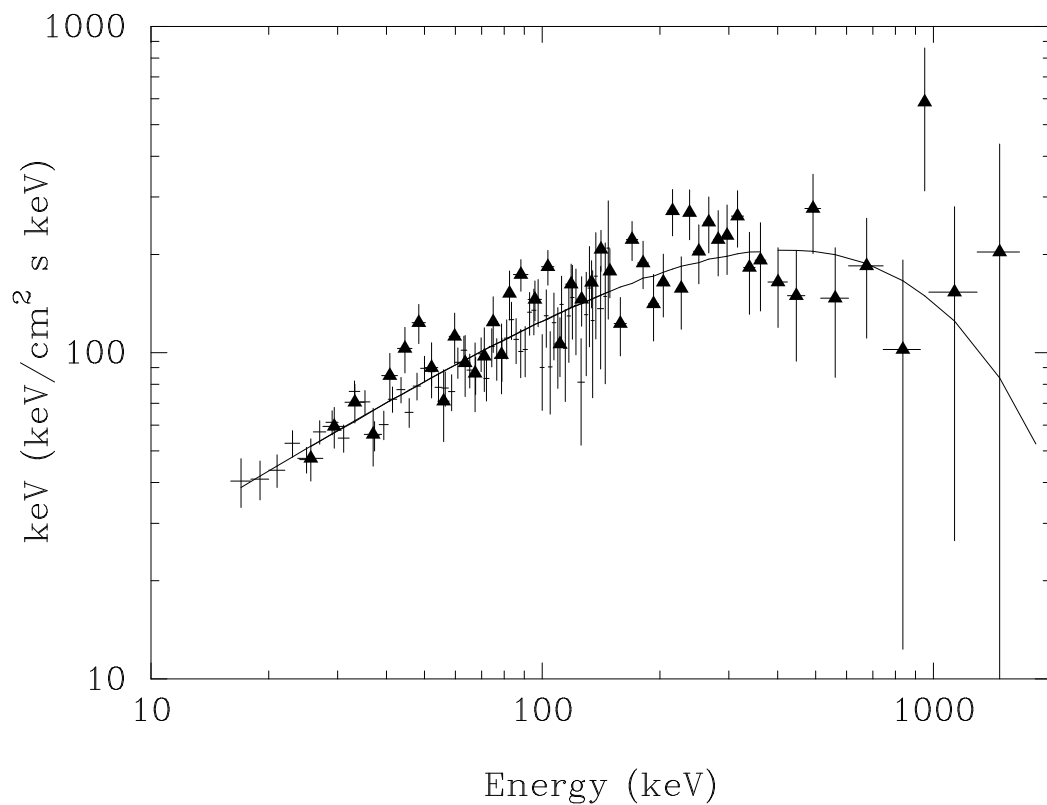


Fig. 2.— Plot of Konus-Wind data in 3 bands and associated band ratios during burst prompt emission. Data binning is 64ms.



val 11-Dec-2005 21:53

Fig. 3.— Plot of joint spectral energy distribution of Konus-Wind and BAT data during burst prompt emission, showing E_{peak} at ~ 440 keV. K-W data are filled triangles, BAT data are crosses.

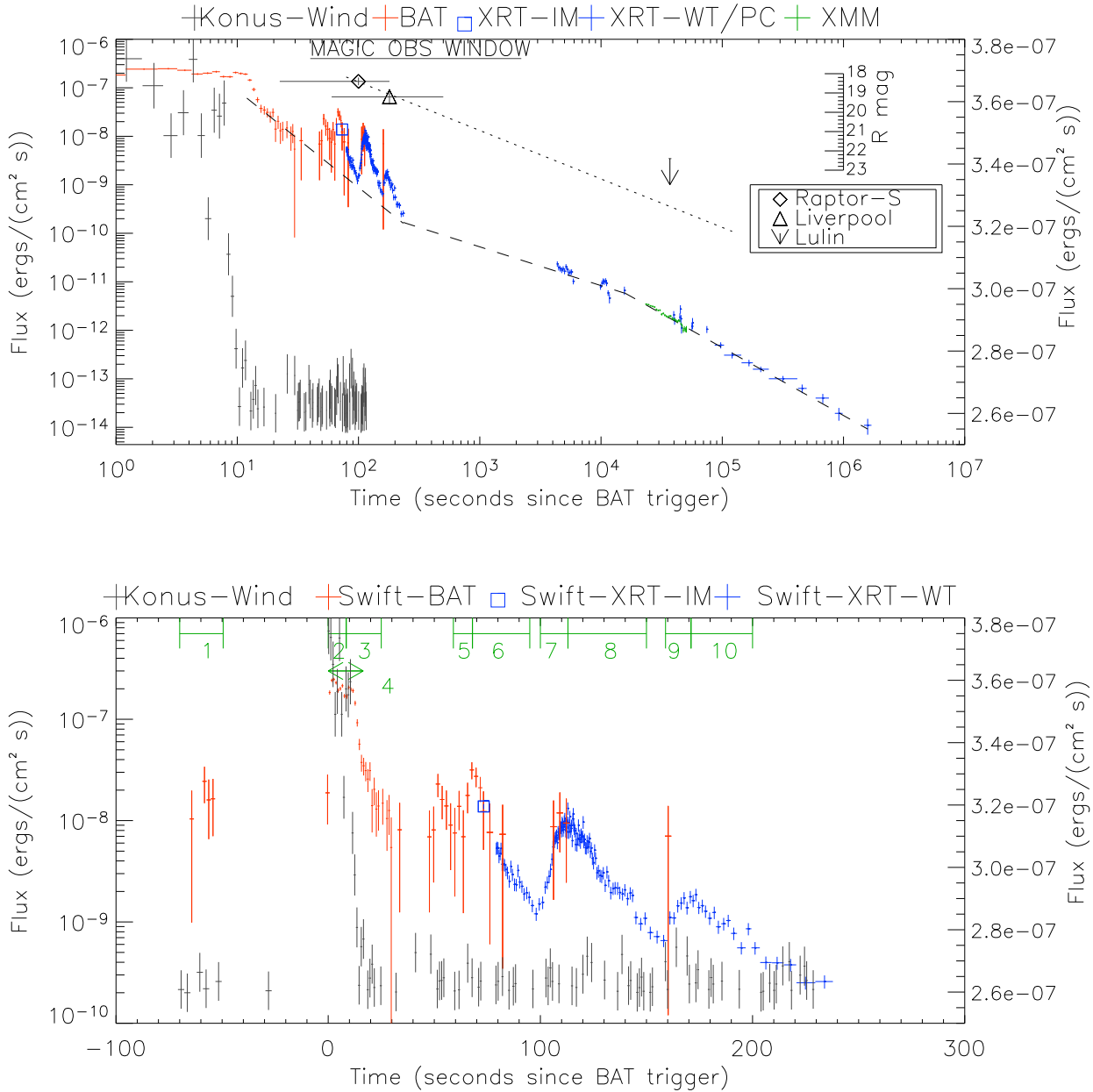


Fig. 4.— X-ray/ γ -ray/optical lightcurve of GRB 050713A. Top: multicolored points are *Swift* and XMM data scaled to the left Y-axis. Black crosses are K-W data scaled to the right Y-axis. Fluxes are extrapolated into the 0.2-10 keV energy range. The diamond, cross and arrow are optical observations and scaled to the inset Y-axis. The scaling of the inset Y-axis is consistent with the outer, left Y-axis in that 1 magnitude is equal to a factor of 2.5 in flux. The window of MAGIC observations is shown by the horizontal bar. The dashed line is the supposed underlying powerlaw decay. Data from T_0+4 ks to T_0+16 ks are well fit by a powerlaw of slope t^{-1} , implying an energy injection phase. A break to a steeper decay of $t^{-1.45}$ occurs between T_0+16 ks and T_0+40 ks. We note the similar decay slopes in each of the three flares seen by XRT. Optical data are plotted with a fitted powerlaw decay of $t^{-1.0}$. Bottom: a close-up of the flares. Green bars indicate the segments of joint spectral fits.

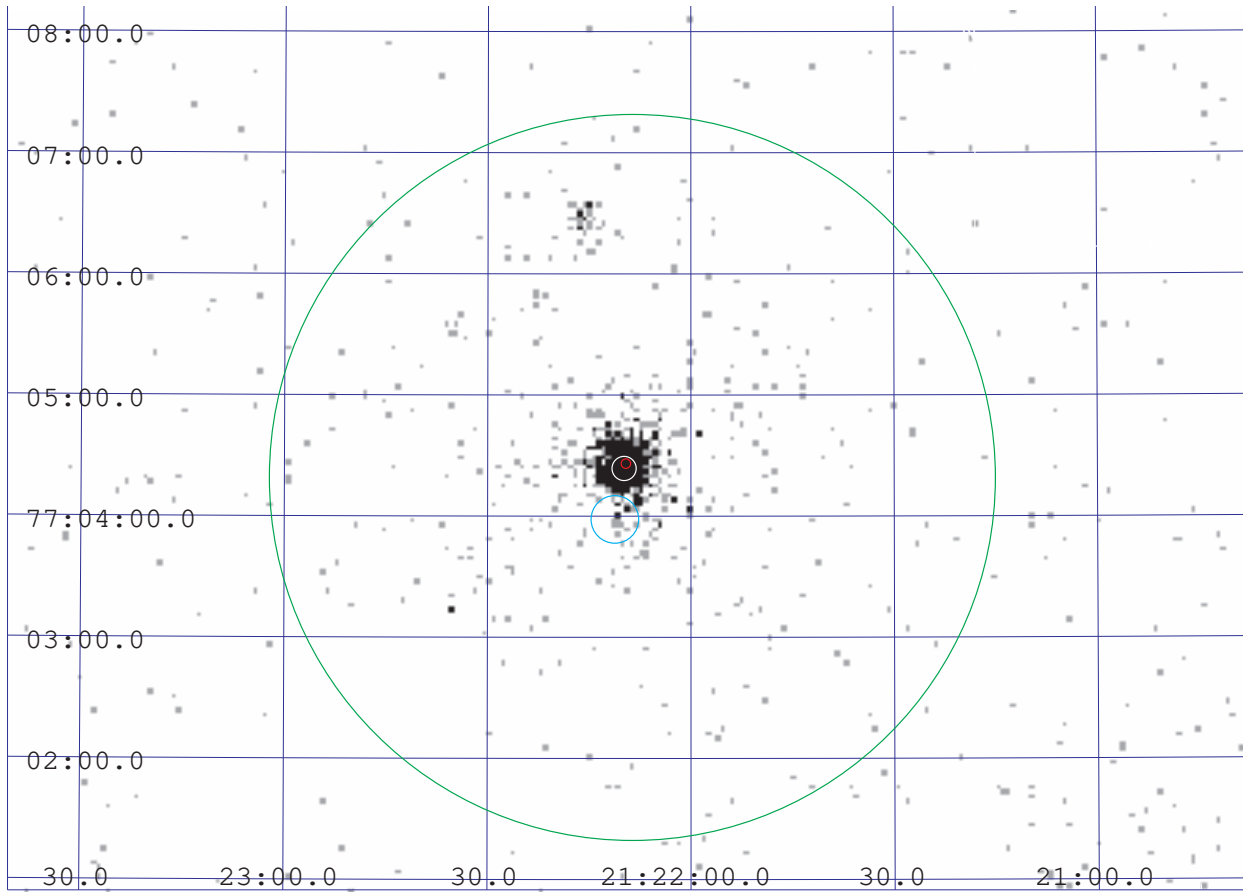


Fig. 5.— XRT image with BAT, XRT optical error circles plotted. green = BAT, dark white=XRT, red=optical. The light blue circle indicates the location of the serendipitous source located 30 arcseconds south of the GRB which has been subtracted from the data.

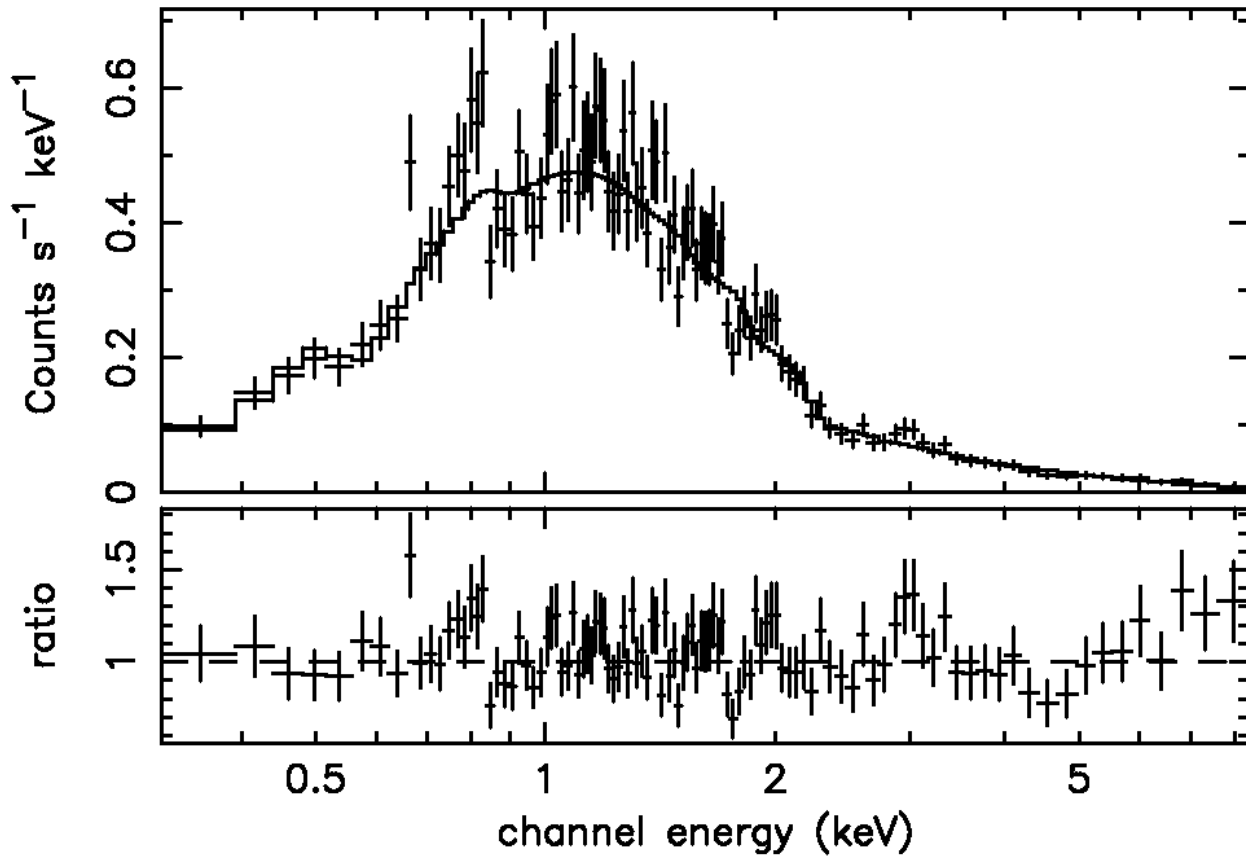


Fig. 6.— PN spectrum from the first 8ks of the *XMM-Newton* observation. The top panel shows the PN data (crosses) with best fit model (solid line) overlaid, which consists of an absorbed power-law of $\Gamma = 2.07$ and $N_{\text{H}} = 3.2 \times 10^{21} \text{ cm}^{-2}$. The bottom panel shows the data/model ratio residuals to this continuum model. A weak excess of counts is seen near 0.8 keV and 3 keV, although if interpreted as emission lines, the detection is only weak at 99% significance.

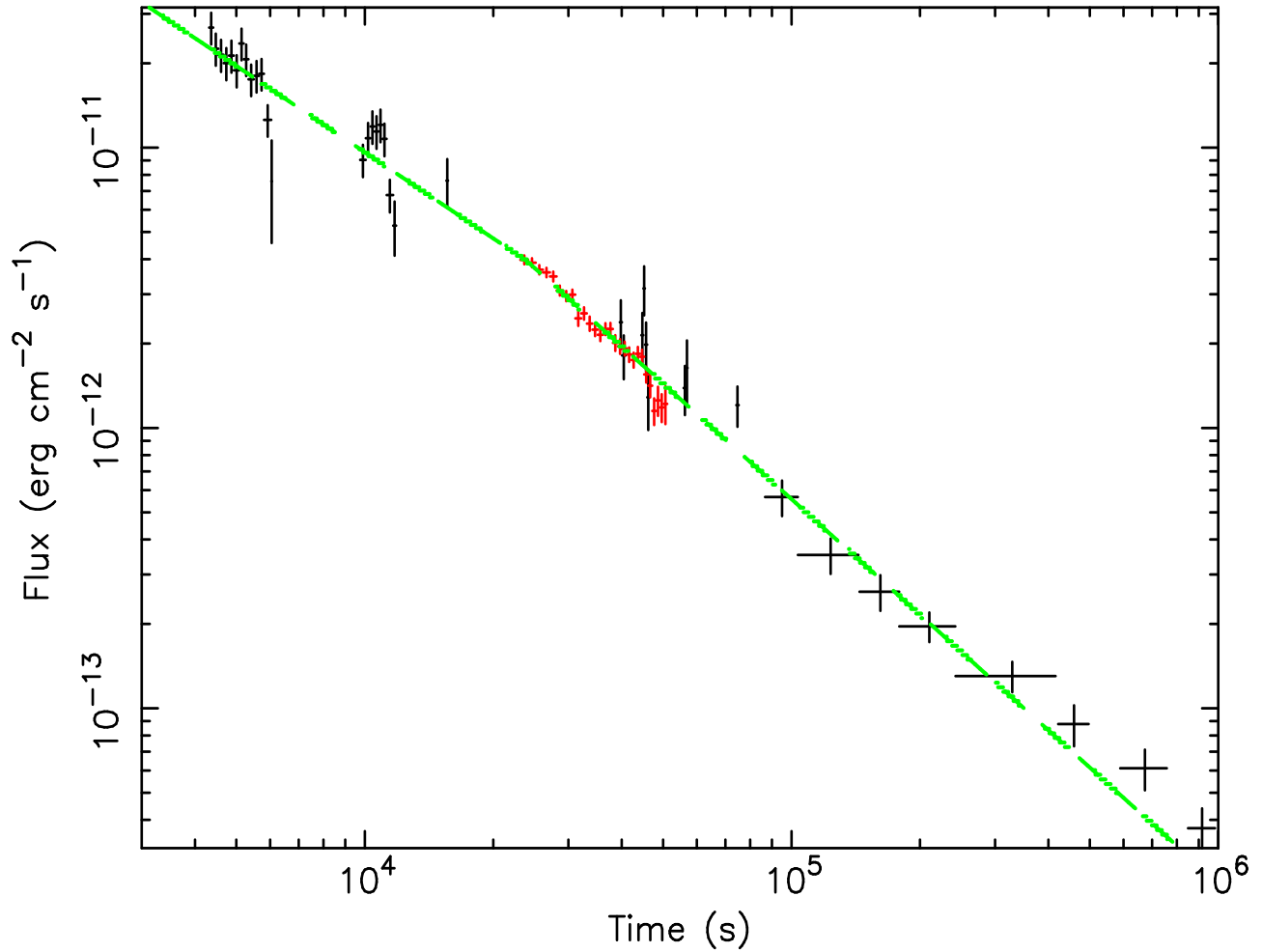


Fig. 7.— Joint *Swift* XRT and *XMM-Newton* PN lightcurve from the 2nd orbit of *Swift* data 4000 s after the BAT trigger, until 10^6 s after the burst. *Swift* XRT points are shown in black, *XMM-Newton* as red. The afterglow flux is measured in 0.5–10 keV band, not correcting for absorption. The solid line plotted to the different segments of data is a broken power-law decay model, outlined in the text. The *XMM-Newton* decay index ($\alpha = 1.45$) is considerably steeper than in the XRT at earlier times ($\alpha = 1.0$), suggesting that a break occurs in the lightcurve decay at around 25 ks.

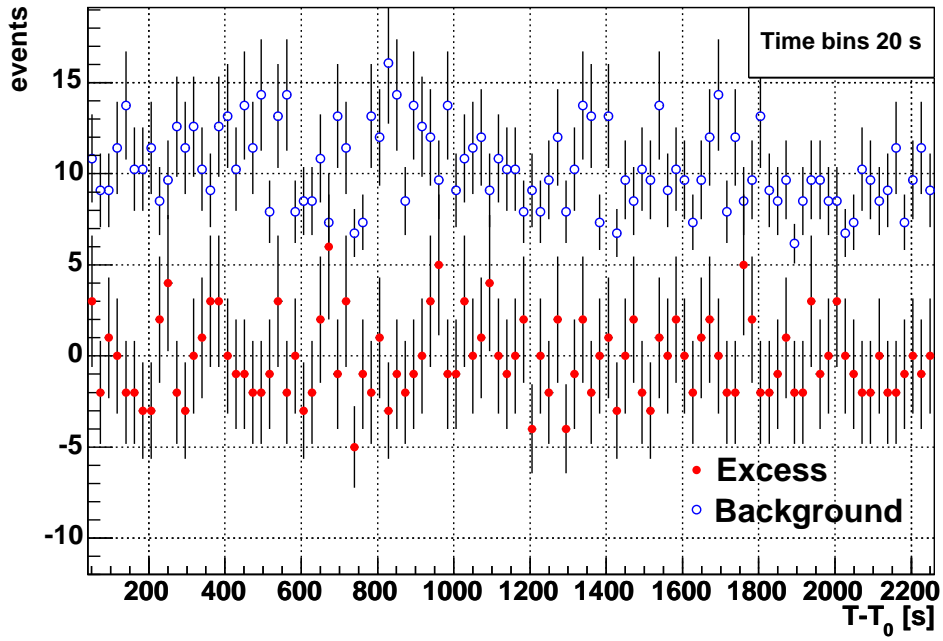


Fig. 8.— MAGIC Observations. Full circles- number of excess events for 20 s intervals, in the 37 min window after the burst onset. Open circles- number of background events in the signal region.

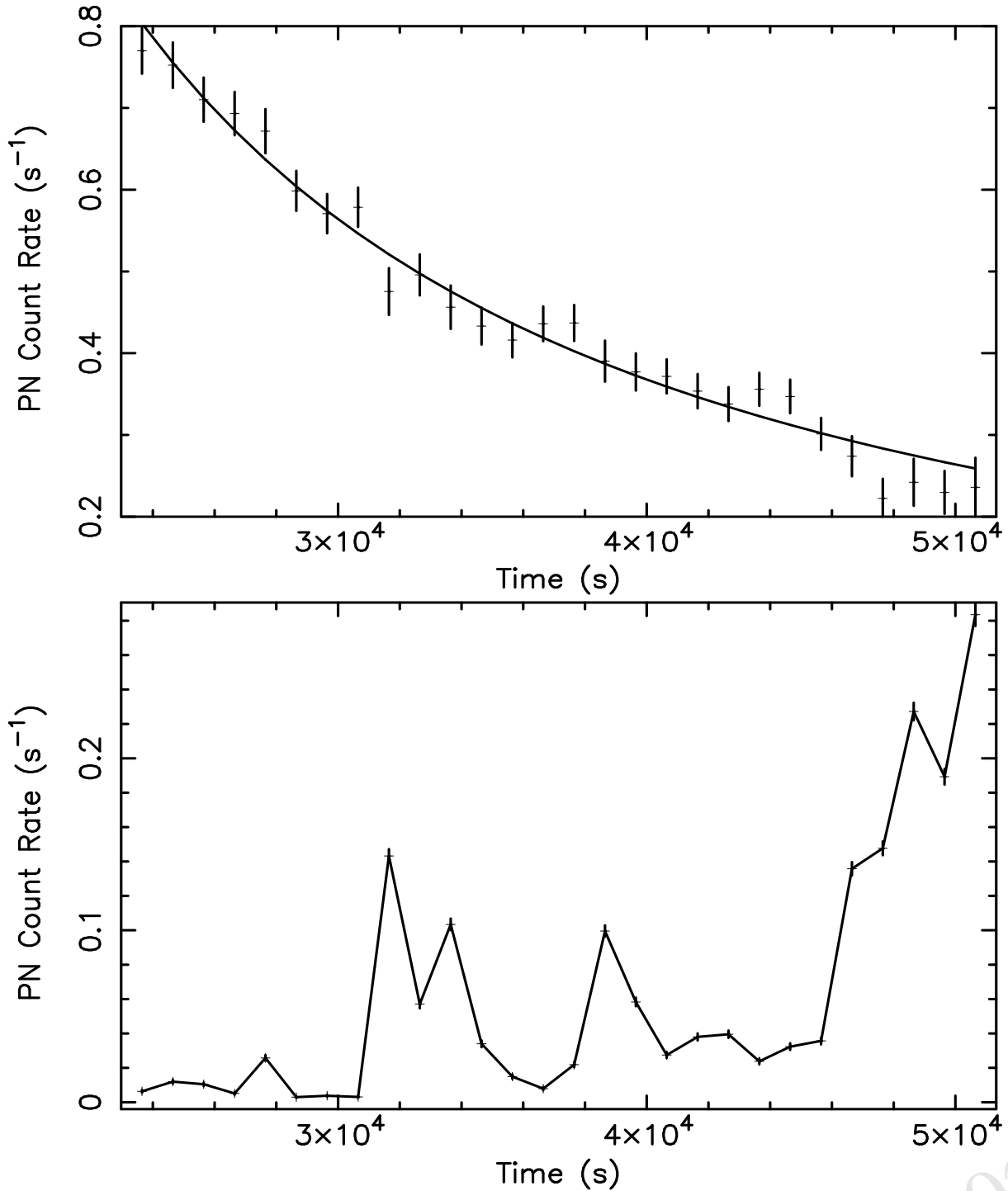


Fig. 9.— *XMM-Newton* lightcurves for the afterglow of GRB 050713A. The top panel shows the background subtracted afterglow lightcurve for the PN detector. Crosses show the GRB source counts (1σ errors), the solid line shows the best fit decay rate of $t^{-1.45}$. Time is plotted compared to the initial BAT trigger. The bottom panel shows the background lightcurve for the PN, normalized to the size of the source extraction region for comparison.

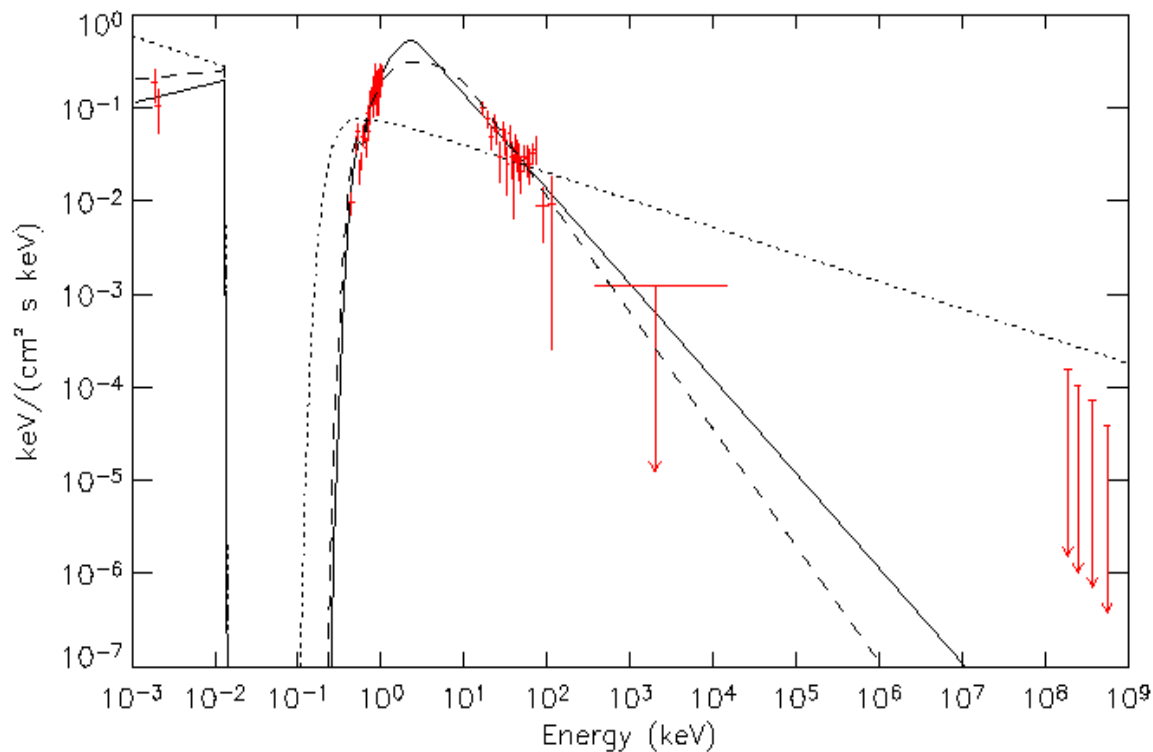


Fig. 10.— Combined multi-platform SED of the early afterglow of GRB 050713A from T_0+30s to T_0+300s . Optical data are from RAPTOR-S at LANL and the Liverpool robotic telescope, soft X-ray (0.2-10keV) data are from *Swift* XRT, hard X-ray (15-150keV) data are from *Swift* BAT and gamma-ray upper limits are from Konus-Wind (0.5-20MeV) and MAGIC (175-500GeV). The three lines plotted over the data represent the 3 models discussed as proposed fits to the SED in the text. The absorbed broken power law (solid) and absorbed Band function (dashed) are both acceptable fits to the broadband SED. The simple absorbed powerlaw (dotted) does not appear reconcilable with the data.